Monthly Notices of the ROYAL ASTRONOMICAL SOCIETY

MNRAS **501,** 2810–2820 (2021) doi:10.1093/mnras/staa3247
Advance Access publication 2020 October 23

Extracting galaxy merger time-scales II: a new fitting formula

R. J. J. Poulton [1,2]★ C. Power [1,2] A. S. G. Robotham [1,2] P. J. Elahi [1,2] and C. D. P. Lagos [1,2]

[1]*International Centre for Radio Astronomy Research, University of Western Australia, 35 Stirling Highway, Crawley, WA 6009, Australia*
[2]*ARC Centre of Excellence for All Sky Astrophysics in 3 Dimensions (ASTRO 3D)*

Accepted 2020 October 15. Received 2020 October 14; in original form 2020 June 28

ABSTRACT

Predicting the merger time-scale ($\tau_{\rm merge}$) of merging dark matter haloes, based on their orbital parameters and the structural properties of their hosts, is a fundamental problem in gravitational dynamics that has important consequences for our understanding of cosmological structure formation and galaxy formation. Previous models predicting $\tau_{\rm merge}$ have shown varying degrees of success when compared to the results of cosmological *N*-body simulations. We build on this previous work and propose a new model for $\tau_{\rm merge}$ that draws on insights derived from these simulations. We find that published predictions can provide reasonable estimates for $\tau_{\rm merge}$ based on orbital properties at infall, but tend to underpredict $\tau_{\rm merge}$ inside the host virial radius (R_{200}) because tidal stripping is neglected, and overpredict it outside R_{200} because the host mass is underestimated. Furthermore, we find that models that account for orbital angular momentum via the circular radius $R_{\rm circ}$ underpredict (overpredict) $\tau_{\rm merge}$ for bound (unbound) systems. By fitting for the dependence of $\tau_{\rm merge}$ on various orbital and host halo properties, we derive an improved model for $\tau_{\rm merge}$ that can be applied to a merging halo at any point in its orbit. Finally, we discuss briefly the implications of our new model for $\tau_{\rm merge}$ for semi-analytical galaxy formation modelling.

Key words: methods: numerical – galaxies: evolution – galaxies: haloes.

1 INTRODUCTION

The idea that galaxies are embedded in massive, gravitationally bound, haloes of dark matter was first proposed in the 1970s (e.g. Freeman 1970), based on observations of the rotation curves of spiral galaxies. Subsequent observational evidence (e.g. Faber & Jackson 1976; Rubin et al. 1980) helped to establish dark matter as the 'scaffolding of the Universe' (cf. Dayal & Ferrara 2018), tracing the distribution of galaxies and the cosmic web, and ultimately this led to the emergence of the hierarchical cold dark matter (CDM) model of structure formation. In the CDM model, low-mass dark matter haloes form via gravitational collapse and merge with other haloes to grow progressively more massive structures. An integral part of this process is that merging haloes must lose orbital energy and angular momentum to sink to the centre of the more massive host halo before it merges completely. At this point, the merging halo, and any galaxy that resides in it, is subsumed into the larger halo and is no longer distinct (Toomre 1977; White & Rees 1978; Blumenthal et al. 1986).

Estimating how long this process takes – from the point at which a merging system first crosses the virial radius of its more massive host, to the point at which it is disrupted and is no longer a distinct, gravitationally bound, entity – is a theoretical problem of fundamental importance. This is most evident in semi-analytical models (SAMs) of galaxy formation and evolution (see Baugh 2006; Benson 2010; Somerville & Davé 2015), which assume physical prescriptions for galaxy formation that link to the assembly history of haloes parametrized in the form of merger trees, which are most commonly drawn from cosmological *N*-body simulations (Cole et al. 2002; Baugh 2006; Srisawat et al. 2013; Lee et al. 2014). The time-scale for haloes and the galaxies they host to merge will impact their predicted properties, and so an accurate merger time-scale is essential. However, finite numerical resolution limits the ability of *N*-body simulations to track haloes into high overdensity regions over many orbits and, consequently, to predict the time-scale on which merging occurs (e.g. Ostriker et al. 1972; Gnedin, Hernquist & Ostriker 1999; Dekel, Devor & Hetzroni 2003; Hayashi et al. 2003; Kravtsov, Gnedin & Klypin 2004; Taylor & Babul 2004; D'Onghia et al. 2010; van den Bosch & Ogiya 2018; van den Bosch et al. 2018). This has led to the use of the merger time-scale ($\tau_{\rm merge}$) in SAMs to predict when poorly resolved haloes merge. As a result, it has been explored extensively to understand the physical properties that govern it, which are formalized in models deduced analytically or from fits to simulation data, and how it impacts galaxy mergers (e.g. Binney & Tremaine 1987; Lacey & Cole 1993; Navarro, Frenk & White 1995; Colpi, Mayer & Governato 1999; Velazquez & White 1999; Jiang & Binney 2000; Taffoni et al. 2003; Zentner et al. 2005; Boylan-Kolchin, Ma & Quataert 2008; Jiang et al. 2008; Gan et al. 2010; Mo, van den Bosch & White 2010; Wetzel & White 2010; Jiang et al. 2014; Simha & Cole 2017).

The merger time-scale was first formulated analytically by Binney & Tremaine (1987[1]; BT87 hereafter), which is based on Chan-

[1]We note that both the Binney & Tremaine (1987) and Lacey & Cole (1993) models are not formally for $\tau_{\rm merge}$ because their focus is dynamical friction only, and not the variety of processes that are present in an *N*-body simulation. However, we include them in our work because they have been used as a proxy for $\tau_{\rm merge}$ in some SAMs.

★ E-mail: rhys.poulton@research.uwa.edu.au

drasekhar's dynamical friction prescription (Chandrasekhar 1943) – the primary (but not sole) mechanism by which haloes lose their orbital energy (Boylan-Kolchin et al. 2008; Jiang et al. 2008). This formulation assumes that the infalling halo (or subhalo once it crosses the host virial radius $R_{\rm vir,\,host}$) is a point mass, moving at velocities much less than the local velocity dispersion of the host through a uniform background of low-mass point masses. Subsequently, Lacey & Cole (1993[1]; LC93 hereafter) proposed an analytical model that treats the host halo as a singular isothermal sphere and integrates the orbit-averaged equations to find the $\tau_{\rm merge}$ based on the initial orbital energy and orbital angular momentum. This inclusion of energy and angular momentum, through use of the circularity (η) and circular radius ($R_{\rm circ}$),[2]means that this formulation can account for varying orbits.

Following on from the analytical work of BT87 and LC93, Jiang et al. (2008; hereafter J08) and Boylan-Kolchin et al. (2008; hereafter BK08) used numerical simulations to refine models for $\tau_{\rm merge}$. J08 investigated the performance of the LC93 formulation by comparing its predictions with hydrodynamical *N*-body simulations, and found that it systematically underpredicts the time-scale for minor mergers and overpredicts it for major mergers, which they distinguish by a 3:1 mass ratio. This led them to propose a new model for $\tau_{\rm merge}$ by fitting to the simulations as a function of η and $R_{\rm circ}$. At the same time, BK08 use idealized simulations of a host halo and merging satellite, run with different mass ratios, η and $R_{\rm circ}$, to assess how orbital energy and angular momentum modifies $\tau_{\rm merge}$ as formulated by BT87. This led them to obtain a fit to $\tau_{\rm merge}$ from their simulations by parametrizing the dependence on host-to-satellite mass ratio, η and $R_{\rm circ}$.

In the preceding paper in this series (Poulton et al. 2019), we used accurate merger trees to characterize the orbital properties of the (sub)halo population in cosmological *N*-body simulations, and assessed the performance of the models proposed by BT87, LC93, J08, and BK08 for predicting $\tau_{\rm merge}$. We concluded that all the considered models provide a reasonable approximation for systems with short-to-intermediate $\tau_{\rm merge}$, but they tend to overpredict $\tau_{\rm merge}$ for the smallest mass systems. Moreover, the values for $\tau_{\rm merge}$ that are based on models derived from simulations (J08 and BK08) perform well when predicting $\tau_{\rm merge}$ for subhalos whose properties are comparable to those used in the original studies – principally set by the number of particles in a subhalo and its mass ratio relative to its host – but tend overpredict it by a factor of 100 when we consider subhalos with higher mass ratios, probing a regime that could not be resolved in the original studies.

In this paper, we investigate the physical factors that underpin the various models for $\tau_{\rm merge}$ to understand what drives their performance in the various regimes, and what gives rise to the discrepant behaviours highlighted in Poulton et al. (2019). We propose a new, more accurate, model for $\tau_{\rm merge}$ that includes the effects of dynamical friction, dynamical self-friction (Miller et al. 2020), tidal stripping, and tidal heating. This new model is applicable to a large dynamic range of subhalo or satellite mass to host mass ratios, in a large variety of environments, and can be applied at any point in a subhalo's or satellite's orbit around its host.

[2]Recall that the circularity is defined as, $\eta = J_{\rm halo}/J_{\rm circ}(E)$, where $J_{\rm halo}$ is the specific angular momentum of the orbiting (sub)halo and $J_{\rm circ}(E)$ is the specific angular momentum of the equivalent circular orbit with the same energy (E). The corresponding circular radius is $R_{\rm circ} = GM_{\rm encl,host}(r)M_{\rm sub}/2E$, where $M_{\rm sat}$ is the subhalo mass and $M_{\rm encl,\,host}(r)$ is the enclosed mass at the radius of the subhalo.

The remainder of this paper is organised as follows: in Section 2, we describe the input simulation, the calculations used, and the sample of subhalos and hosts that we use in our analysis. In Section 3, we discuss the current $\tau_{\rm merge}$ predictions; we present our new model; and we assess its performance compared to the current prescriptions. Finally, in Section 4, we discuss our results, and we present our conclusions and their implications. Throughout this paper, we use virial quantities for the host halo, which are defined using $200\rho_{\rm crit}$, where $\rho_{\rm crit}$ is the critical density of the Universe.[3] We assume a ΛCDM cosmology in accordance with the Planck Collaboration data (Alves et al. 2016) – with density parameters $\Omega_M = 0.3121$, $\Omega_b = 0.6879$, and $\Omega_\Lambda = 0.6879$; a normalization $\sigma_8 = 0.815$; a primordial spectral index $n_s = 0.9653$; and $\rm H_0 = 67.51 km\,s^{-1}Mpc^{-1}$. Note that we use the terms subhalo and satellite interchangeably in this paper.

2 METHODS

2.1 Simulations and halo tracking

The simulations used in this work come from the GENESIS suite of *N*-body simulations, with volumes ranging from 26.25 to 500 Mpc h^{-1} and between 324^3 and 5200^3 particles. We focus on the 105 h^{-1} Mpc box with 2048^3 particles simulation because it allows us to probe well-resolved hosts ranging in mass from 10^{12} to $10^{14}M_\odot$. This simulation has a total of 190 snapshots, evenly spaced in logarithmic expansion factor ($a = 1/(1+z)$) between $z = 24$ to $z = 0$. This high cadence (on average 70 Myr between snapshots) enables an accurate capturing of the evolution of dark matter haloes and their orbits.

Halo catalogues are constructed using VELOCIRAPTOR, a 6D Friends-of-Friends (6D-FoF) phase space halo finder (Elahi, Thacker & Widrow 2011; Elahi et al. 2013; Poulton et al. 2018; Cañas et al. 2019; Elahi et al. 2019a), while trees are constructed using TREEFROG (Poulton et al. 2018; Elahi et al. 2019b), which is a particle correlator that can link across multiple snapshots and halo catalogues. Importantly, TREEFROG's ability to link across multiple snapshots is vital for tracking subhalos as they orbit within highly overdense regions. While a subhalo may not be present in a pair of halo catalogues at consecutive output times, it may be present in halo catalogues at a later time, and so there might be gaps in the subhalo's history. This has led to the development of the halo tracking tool known as WHEREWOLF, as described in (Poulton et al. 2018, 2019). WHEREWOLF is a halo ghosting tool, designed to fill in the gaps in a subhalo's history using the particles from the simulation and attempting to find the missing halo using the subhalo's bound particles and calculating its properties. WHEREWOLF also attempts to extrapolate when the halo merges, so that subhalos are tracked until they coalesce with their host.

To extract all subhalos relative to their host and calculate their orbital properties, we use ORBWEAVER as described in Poulton et al. (2019). ORBWEAVER first identifies host haloes of interest; identifies (sub)haloes that come within $\rm N \times R_{vir,\,host}$; extracts the full history of the (sub)halo relative to its host; identifies key points in its orbit; before finally interpolating the orbit to obtain characteristic properties of the orbit at these key points. Using ORBWEAVER we calculate $\tau_{\rm merge}$ as being the exact time from infall (crossing $R_{\rm vir,\,host}$) to the time when the halo is no longer a self-bound entity (has phase mixed with its host).

[3]We could use other definitions of host halo mass and radius, which would change some parameters in our model.

2.2 Calculating orbital properties

We calculate halo/subhalo positions and velocities (in physical coordinates and including the Hubble flow) relative to the centre of potential of the host. We compute halo/subhalo orbital properties by treating them as isolated point particles in the reduced mass frame, while separations and relative velocities with respect to the host are calculated as $\boldsymbol{r} = \boldsymbol{r}_{\rm host} - \boldsymbol{r}_{\rm sat}$ ($\boldsymbol{v} = \boldsymbol{v}_{\rm host} - \boldsymbol{v}_{\rm sat}$). The reduced mass is $\mu = M_{\rm sat} M_{\rm encl,\,host}(r)/(M_{\rm sat} + M_{\rm encl,\,host}(r))$, where $M_{\rm sat}$ is the mass of the subhalo and $M_{\rm encl,\,host}(r)$ is the enclosed mass of the host out to radius r, which is calculated assuming a Navarro, Frenk and White (NFW) profile (Navarro, Frenk & White 1997), with a characteristic density[4] given by

$$\rho_0 = \frac{M_{\rm vir,host}}{4\pi R_{\rm s}^3 \left[\ln(1+c) - \left(\frac{c}{1+c}\right)\right]}. \quad (1)$$

Here, c is the NFW concentration parameter $c = \frac{R_{\rm vir}}{R_{\rm s}}$. $\rm M_{encl,\,host}$ is given by

$$M_{\rm encl,host}(r) = 4\pi\rho_0 R_{\rm s}^3 \left[\ln\left(1+\frac{r}{R_{\rm s}}\right) - \left(\frac{r}{R_{\rm s}+r}\right)\right] \quad (r < R_{\rm vir,host}) \quad (2)$$

$$M_{\rm encl,host}(r) = M_{\rm vir,host} \qquad (r \geq R_{\rm vir,host}). \quad (3)$$

The orbital energy of the subhalo[5] is given by

$$E = 0.5\mu v^2 - \frac{G M_{\rm encl,host}(r) M_{\rm sat}}{r}, \quad (4)$$

and its orbital angular momentum is

$$L = \mu \boldsymbol{r} \times \boldsymbol{v}. \quad (5)$$

The eccentricity of the orbit can be computed from

$$e = \sqrt{1 + \frac{2EL^2}{(G M_{\rm encl,host}(r) M_{\rm sat})^2 \mu}}, \quad (6)$$

and the pericentric distance from the host centre is given by

$$R_{\rm peri} = \frac{L^2}{(1+e) G M_{\rm encl,host}(r) M_{\rm sat} \mu}. \quad (7)$$

It is also possible to compute the dynamical time of a subhalo at radius r assuming

$$T_{\rm dyn}(r) = \sqrt{\frac{r^3}{G M_{\rm encl,host}(r)}}. \quad (8)$$

2.3 Merging sample

2.3.1 Selection criteria

Our goal is to create an analytical formulation for $\tau_{\rm merge}$ for objects that merge with their host,[6] but to ensure that we have objects that can be treated (to first order) as members of two-body systems (so equation 7 can be applied), we apply the same selection as presented Poulton et al. (2019) to select our hosts:

Top of its spatial hierarchy: This excludes satellites orbiting satellites, which make up a negligible number of the orbiting sample.

$N_{host} > 10\,000$ particles: The host potential must be well sampled, so that orbital histories for the orbiting systems can be accurately recovered.

These selection criteria guarantee that our host selection contains well-resolved field haloes and removes any satellite–satellite mergers (which represent only 10 per cent of mergers in a typical simulation; see Deason, Wetzel & Garrison-Kimmel 2014).

Ideally, we would like to track satellites until they coalesce physically with their hosts, but finite time sampling and insufficient numerical resolution means that satellites can disrupt and coalesce unphysically with their host before this point. To circumvent these issues, we first select systems that satisfy (see Appendix D for how these were selected):

Merge within 0.1 $R_{\rm vir,host}$A satellite must be within 0.1 $R_{\rm vir,host}$ when it is lost, and be a secondary progenitor of its host.

$N_{\rm sat} > 1000$ particles at infallHalos that are satellite progenitors cannot disrupt before they come within $R_{\rm vir,host}$ (cf. van den Bosch & Ogiya 2018).

Finally, we require that systems must satisfy at all times:

$N_{\rm sat} > 100$ particles: The mass of the satellite must be well above the threshold for detection by the halo finder.

$R_{\rm s} > 2.0 \times$ softening length:The satellite is sufficiently well resolved in the simulation such that it is not susceptible to artificial disruption due to force softening.

These criteria result in 8930 mergers in our simulation that we can use in our analysis. We use every point between 0.1 and 3.0 $R_{\rm vir,host}$ in the merging system's orbital history.

2.3.2 Sample distributions

Fig. 1 shows the basic statistical properties of the merging sample, as well as for all systems that survive until $z = 0$ in our selected hosts. In our merging sample, there are two times more minor mergers than major mergers, where we split major to minor at a 3:1 mass ratio. Systems that merge tend to have mass ratios closer to 1:1 than systems that survive. The surviving sample falls on to the host later than the merging sample, with median infall redshifts of $z_{\rm infall} \simeq 1.5$ for the merging sample and $z_{\rm infall} \simeq 0.5$ for the surviving sample. This difference in median infall redshift indicates that it is interaction with the host environment rather than intrinsic properties of the infalling systems that drives merging.

The merging sample tends to be on more radial orbits compared to the surviving sample, with a median of 0.45 for merging systems and 0.7 for surviving systems, and they also tend to have smaller values of $R_{\rm peri}/R_{\rm vir,\,host}$, with a median of 0.2 compared to 0.45 for the surviving sample. This difference between merging and surviving samples suggests the predictive capability of $R_{\rm peri}$ for determining mergers in the time of the simulation.

3 A NEW MODEL FOR THE MERGER TIME-SCALE

In this section, we evaluate how commonly used published formulae (cf. Table 1) for $\tau_{\rm merge}$ – from BT87, LC93, J08, BK08 – perform as a function of $r/R_{\rm vir,\,host}$, and present our new formulation for $\tau_{\rm merge}$ and its variation with $r/R_{\rm vir,\,host}$. We also discuss the dependence of $\tau_{\rm merge}$ on orbital energy.

[4]This is a property of the halo.
[5]We note that the following equation is for a point mass, but it provides a good approximation and is a efficient means of calculating the orbital state.
[6]We consider all merger events up to $z = 0$ to maximize statistics.

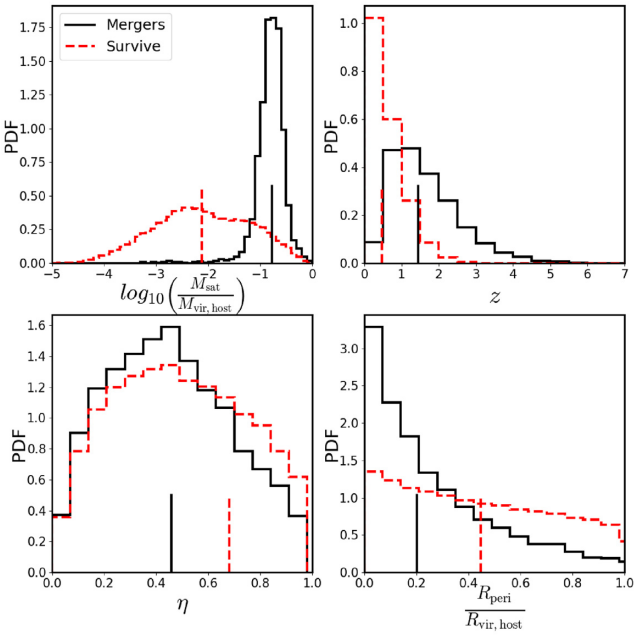

Figure 1. The basic statistical properties of the merging sample calculated at infall. *Top left*: the mass ratio between the satellite and the host. *Top right*: the redshifts where these objects are found. *Bottom left*: circularity η. *Bottom right*: the ratio of $R_{\rm peri}$ from equation 7 to $R_{\rm vir,host}$. The solid black line shows the distribution for the merging sample and the dashed red line shows the sample that survives until z=0. The vertical black and dashed red lines shows the medians of the distributions.

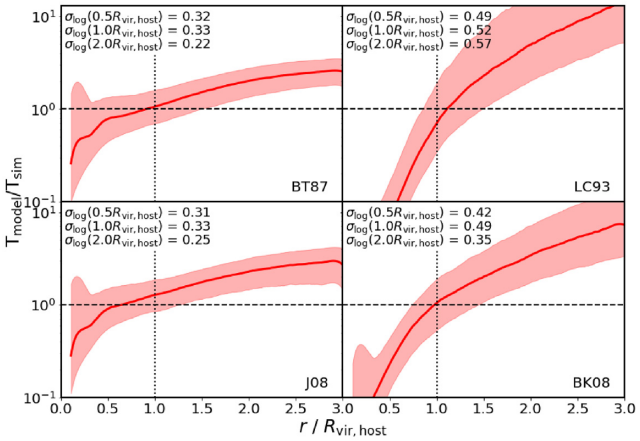

Figure 2. The ratio of the existing $\tau_{\rm merge}$ prescriptions predictions ($T_{\rm model}$) to the measured $\tau_{\rm merge}$ from the simulation ($T_{\rm sim}$) change as a function of $r/R_{\rm vir,host}$. The text in the bottom right of each panel states the $T_{\rm model}$ that is shown. The red line shows the median of the population and the shaded region show the standard deviation. The text in the top left of each panel states the standard deviation in $T_{\rm model}/T_{\rm sim}$ at 0.5, 1.0, and 2.0 $R_{\rm vir,host}$.

3.1 Performance of published models

We compute predictions for $\tau_{\rm merge}$ for merging systems at all points along their orbits and compare with $\tau_{\rm merge}$ measured directly from the orbital history deduced from the merger tree data. In practice, we evaluate the ratio, $T_{\rm model}/T_{\rm sim}$, of the time-scale predicted by the model, $T_{\rm model}$, and the measured simulation time-scale, $T_{\rm sim}$, and show how this varies with $r/R_{\rm vir,\,host}$ in Fig. 2.

3.1.1 Binney & Tremaine (1987; BT87)

We find that the BT87 model recovers $T_{\rm model}/T_{\rm sim} \simeq 1$ when evaluated at $r = R_{\rm vir,\,host}$, but tends to underpredict $\tau_{\rm merge}$ for $r < R_{\rm vir,\,host}$ and overpredict it at $r > R_{\rm vir,\,host}$. The underprediction at smaller radii arises because the model neglects the effects of tidal stripping, which can prolong the lifetime of a satellite (Boylan-Kolchin et al. 2008; Jiang et al. 2008; Mo et al. 2010), whereas the overprediction at larger radii is a consequence of the assumption that accreting haloes are on smoothly inspiralling orbits that do not change as the system falls on to its host. However, this assumption does not hold in practice; most orbits transition from being preferentially radial at larger radii to isotropic within the host (see Appendix A), and so accreting haloes at larger radii take a shorter time to cross the region $1 < r/R_{\rm vir,\,host} < 3$ than predicted by BT87.

3.1.2 Lacey & Cole (1993; LC93)

The LC93 model shows a strong dependence on $r/R_{\rm vir,\,host}$, which reflects its dependence on $R_{\rm circ}$ and η and on the assumption that the virial theorem is valid ($U = 2T$). However, this assumption breaks down when considering systems at the $R_{\rm vir,\,host}$ (see Appendix B for more information) and leads to the large change with $r/R_{\rm vir,\,host}$. The dependence on $r/R_{\rm vir,\,host}$ is exacerbated by the neglect of tidal stripping. Furthermore, the LC93 formula has an offset such that $T_{\rm model}$=$T_{\rm sim}$ at $r = 1.1R_{\rm vir,\,host}$ rather than $r = R_{\rm vir,\,host}$, which is most likely due to the assumption that haloes are isothermal spheres, which leads them to have larger $R_{\rm vir,\,host}$. The LC93 model shows the largest scatter of the models, principally because of the inclusion of $R_{\rm circ}$ and η in its formulation; the scatter is driven by the large range of boundedness of orbits (shown in Appendix B).

3.1.3 Jiang et al. (2008; J08)

The J08 model has the same functional form as the BT87 model, and so it suffers from the same behaviours at small and large radii, with similar scatter. Although J08 calibrated their model using a simulation that naturally accounted for the effects of tidal stripping, the haloes and satellites in their sample covered a restricted mass range, with $M_{\rm sat}/M_{\rm vir,\,host} > 0.1$. This means that their merging systems had smaller $\tau_{\rm merge}$ and so they did not survive sufficiently

Table 1. The published $\tau_{\rm merge}$ prescriptions formulations. The left most column is the $\tau_{\rm merge}$ prescription, the middle column is the parameter values for each prescription and the right most column is the standardized formula used by all these prescriptions.

Model	Parameters					$\tau_{\rm merge}$ formula
BT87	A = 1.17	$\Lambda = 1 + \frac{M_{\rm host}}{M_{\rm sat}}$	b = 1.0	c = 0	$f(\eta) = 1$	$A\left(\frac{T_{\rm dyn}}{\ln(\Lambda)}\right)\left(\frac{M_{\rm host}}{M_{\rm sat}}\right)^{b}\left(\frac{R_{\rm circ}}{R_{\rm vir,host}}\right)^{c} f(\eta)$
LC93	A = 1.17	$\Lambda = \frac{M_{\rm host}}{M_{\rm sat}}$	b = 1.0	c = 2	$f(\eta) = \eta^{0.78}$	
BK08	A = 0.216	$\Lambda = 1 + \frac{M_{\rm host}}{M_{\rm sat}}$	b = 1.3	c = 1	$f(\eta) = \exp(1.9\eta)$	
J08	A = 1.17	$\Lambda = 1 + \frac{M_{\rm host}}{M_{\rm sat}}$	b = 1.0	c = 0	$f(\eta) = 0.94\eta^{0.6} + 0.6$	

long to experience the full effects of tidal stripping. Interestingly, the J08 formula predicts $T_{\rm model} = T_{\rm sim}$ at $r = 0.9R_{\rm vir,\,host}$ rather than $r = R_{\rm vir,\,host}$, which may reflect the use of a hydrodynamical simulation for calibration. This would be consistent with the findings of previous studies, which showed that the inclusion of baryons reduces $\tau_{\rm merge}$ for merging satellites by 10 per cent, (Boylan-Kolchin et al. 2008; Jiang, Jing & Lin 2010). We note that J08 based their results solely on the orbital properties of infalling haloes and satellites at $r = R_{\rm vir,\,host}$, and so did not have information about how their formulation for $\tau_{\rm merge}$ varied with radius.

3.1.4 Boylan-Kolchin et al. (2008; BK08)

The BK08 model is similar to the LC93 model in so far as it accounts for both energy and angular momentum [η, $R_{\rm circ}(E)$] in its formulation. Consequently, it also suffers from the same issues as the LC93 model, albeit to a lesser extent. In common with J08, BK08 based their results solely on the orbital properties of infalling haloes and satellites at r=$R_{\rm vir,\,host}$. Furthermore, they calibrated their model against idealized simulations of merging satellites with their host haloes, and so they did not probe the full range of orbits present in cosmological simulations.

3.2 A new model

In constructing the new model for $\tau_{\rm merge}$, we use the hyperplane fitting package, HYPER.FIT (Robotham & Obreschkow 2015), which uses a likelihood analysis to minimize the scatter in the hyperplane. This allows us to fit a parametrized functional form to the data and to find the key predictive quantities that minimize the scatter in $T_{\rm model}/T_{\rm sim}$.

Our choice of functional form is

$$\mathrm{T_{fit}} = A\ T_{\rm dyn}(r) \left(\frac{r}{R_{\rm vir,host}}\right)^{b} \left(\frac{R_{\rm peri}}{R_{\rm vir,host}}\right)^{c}. \tag{9}$$

This predicts orbits that agree well with the data (see Appendix C) and it accounts for the expected dependence of $\tau_{\rm merge}$ on a satellite's position within its host and the dynamical time of the host. The various physical quantities are as defined in Section 2.2, and A, b, and c are free parameters. With this definition, we favour values of $A = 5.5$ and $c = 0.2$, while the constant b is dependent on the satellite's position – specifically, whether it is inside or outside $R_{\rm vir,host}$.[7] We find

$$\begin{aligned} b &= -0.5 \quad (r < R_{\rm vir,host}),\\ b &= -1.0 \quad (r \geq R_{\rm vir,host}), \end{aligned} \tag{10}$$

which means that there is a stronger dependence on position when outside the host. Equation (9) simplifies to

$$\mathrm{T_{fit}} = 5.5 \sqrt{\frac{R_{\rm vir,host}}{GM_{\rm encl,host}(r)}}\, r^{0.8} R_{\rm peri}^{0.2} \qquad (r < R_{\rm vir,host}), \tag{11}$$

$$\mathrm{T}_{fit} = 5.5\, \frac{R_{\rm vir,host}}{\sqrt{GM_{vir,host}}}\, r^{0.3} R_{\rm peri}^{0.2} \qquad (r \geq R_{\rm vir,host}), \tag{12}$$

which most compactly captures the behaviours at $r < R_{\rm vir,\,host}$ and $r \geq R_{\rm vir,\,host}$.

[7]The extra radial dependence is required inside $R_{\rm vir,\,host}$ due to the use of $M_{\rm encl,\,host}(r)$ that adds an extra radial dependence, which is not present outside $R_{\rm vir,\,host}$ because $M_{\rm vir,\,host}$ is used.

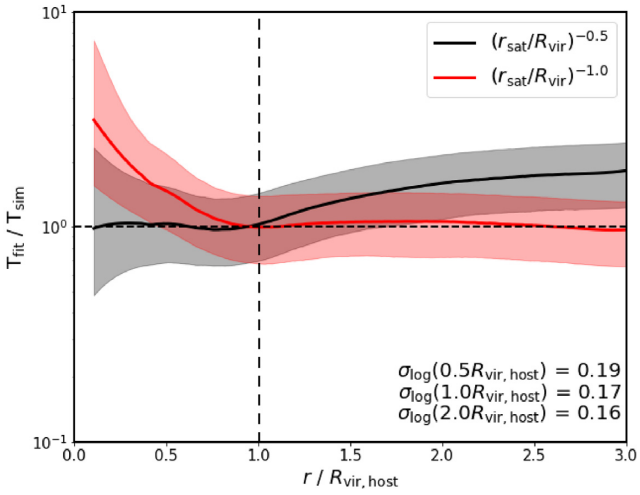

Figure 3. Variation of $T_{\rm fit}/T_{\rm sim}$ with $r/R_{\rm vir,\,host}$. The solid lines show medians of the population, while the shaded region shows the standard deviation. Different colours show the different dependencies of equation (12) on $r/R_{\rm vir,\,host}$, shown in the legend.

3.2.1 Performance

Fig. 3 shows the performance[8] of the new model as a function of $r/R_{\rm vir,\,host}$. Equation (11) performs well at $r < R_{\rm vir,\,host}$ but degrades at $r > R_{\rm vir,\,host}$, while equation (12) performs well at $r > R_{\rm vir,\,host}$ but degrades at $r < R_{\rm vir,\,host}$. This motivates the need for two overlapping formulae to characterize the behaviour of $T_{\rm fit}/T_{\rm sim}$ over the radial range of interest.

We note that the new model has limited dependence on the satellite-to-host mass ratio, such that the dependence on $M_{\rm sat}$[9] is driven by the calculation of $R_{\rm peri}$ from equation (7). However, this dependence on $M_{\rm sat}$ can be removed completely using the specific energy in equation (4) and specific angular momentum in equation (5). Removing this dependence on $M_{\rm sat}$ is useful because the mass of the satellite can depend upon the choice of halo-finder used, particularly for objects deep inside their host potential (Knebe et al. 2011; Muldrew et al. 2012; Poulton et al. 2018).

Removing $M_{\rm sat}$ from equations (11) and (12) yields the specific $\tau_{\rm merge}$ ($T_{\rm new,\,specific}$), given by

$$\mathrm{T_{fit,specific}} = 5.62 \sqrt{\frac{R_{\rm vir,host}}{GM_{\rm encl,host}(r)}}\, r^{0.8} R_{\rm peri,specific}^{0.2} \qquad (r < R_{\rm vir,host}), \tag{13}$$

$$\mathrm{T}_{fit,specific} = 5.62\, \frac{R_{\rm vir,host}}{\sqrt{GM_{vir,host}}}\, r^{0.3} R_{\rm peri,specific}^{0.2} \qquad (r \geq R_{\rm vir,host}), \tag{14}$$

where $R_{\rm peri,\,specific}$ is

$$R_{\rm peri,specific} = \frac{l^2}{(1 + e_{\rm specific}) GM_{\rm encl,host}(r)}, \tag{15}$$

[8]We also demonstrate the performance of the the new model when applied in a lower resolution simulation in Appendix E.

[9]This mass corresponds to both bound and unbound particles, and correspond to particles grouped together by the 6D-FoF algorithm at each simulation output. The mass is the mass of the satellite at the point where the formula is being evaluated.

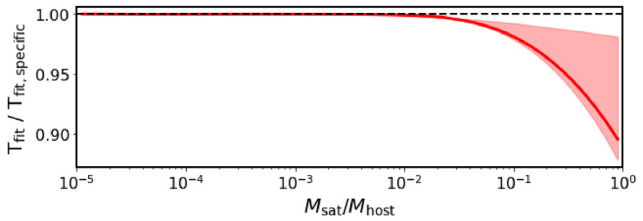

Figure 4. Variation of the ratio of T_{fit} to the specific τ_{merge}, $T_{new,\,specific}$, with the ratio M_{sat}/M_{host}. The red line shows the median of the population and the shaded region shows the standard deviation.

where l is the specific angular momentum and $e_{specific}$ is

$$e_{specific} = \sqrt{1 + \frac{2\varepsilon l^2}{(GM_{encl,host}(r)^2}}, \quad (16)$$

where ε is the specific orbital energy.

To show the effects of using the specific angular momentum and energy, we plot the ratio of T_{fit} to $T_{new,\,specific}$ as a function of M_{sat}/M_{host}. Fig. 4 shows that for most mass ratios there is a good agreement between T_{fit} and $T_{new,\,specific}$, and only starts to overpredict τ_{merge} when M_{sat} is a tenth of M_{host}. The difference is about 10 per cent for the most massive satellites, which is smaller than the differences in the difference in the recovered mass by different halo finders (Knebe et al. 2011).

3.3 Dependence on orbital energy

Fig. 5 shows a 2D histogram of the ratio of T_{model}/T_{sim} plotted against the ratio of orbital kinetic energy (KE) to potential energy relative to its host (GPE), with colour coding accounting for the satellite-to-host mass ratio. This figure shows how the different models perform, even when satellites are currently unbound from their host (i.e. KE > GPE). All of the currently published models (top panels, bottom left-hand panel) tend to underpredict τ_{merge} for larger satellite-to-

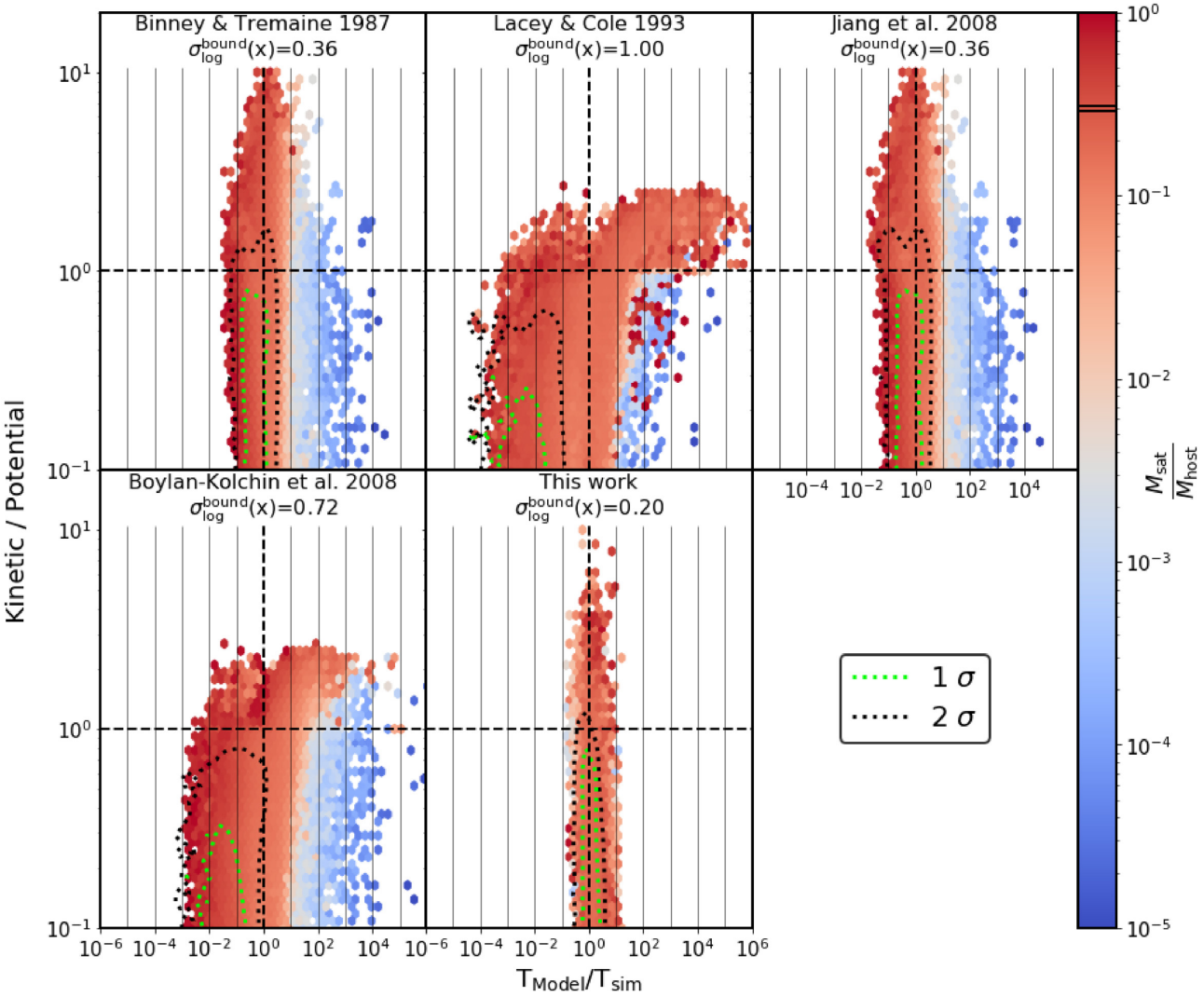

Figure 5. 2D histograms of the joint distribution of the ratio of T_{model} over T_{sim} and the ratio of orbital kinetic energy (KE) to potential energy relative to its host (GPE). The text in the top of each panel states the T_{model} that is shown and the standard deviation of the $\log_{10}(T_{model}/T_{sim})$ for the bound systems in the panel. The horizontal dashed line shows the region that is unbound above and bound below. The vertical dashed line shows where $T_{model} = T_{sim}$. The dotted green and black lines on each panel show the 1σ and 2σ contours, respectively. The colour shows the median satellite-to-host mass ratio in each bin and the box on the colour bar highlights the colour for the median mass of satellites, given no variation in mass.

host mass ratios, and overpredict for smaller mass ratios, reflecting the strong dependence on satellite-to-host mass ratio in the model functional forms.

The Figure also shows that both the LC93 and BK08 models have a dependence on the KE to GPE ratio – when satellites become unbound from the host, $T_{\rm sim}$ tends to be overpredicted. This reflects the dependence of these models on $R_{\rm circ}$, which becomes large when KE $\sim$ GPE (shown in Appendix B). It's also noteworthy that the LC93 model overpredicts the lifetimes of the largest systems (i.e. $M_{\rm sat}/M_{\rm host} \approx 1$) even when they are bound, which arises because the Coulomb logarithm $\log(\Lambda) \rightarrow \infty$ as $M_{\rm sat}/M_{\rm host} \rightarrow 1$.

Our new model (bottom right-hand panel) performs well for all masses and for all types of orbit. As for the BT87 and J08 models, our model's predictions do not change when the satellite becomes unbound. Furthermore, $T_{\rm fit}$ does not show the residual dependence on the satellite-to-host mass shown that was evident in the currently published models. The new model shows reduced scatter, even for the most unbound satellites, which is because it uses $R_{\rm peri}$ to capture the dependence on satellite orbit. We discuss why $R_{\rm peri}$ is a better predictor of orbit than η in Appendix C.

4 CONCLUSIONS

We have investigated the performance of the most commonly used, published, models that predict the time-scale for merging ($\tau_{\rm merge}$) between a satellite and its more massive host [Binney & Tremaine (1987; BK08), Lacey & Cole (1993; LC93), Jiang et al. (2008; J08), and Boylan-Kolchin et al. (2008; BK08)] and used the results of this analysis to motivate a new model based on our own cosmological N-body simulations. Guided by the behaviour of $\tau_{\rm merge}$ predicted by the models inside and outside the more massive host's virial radius, we favour a dual formulation for $\tau_{\rm merge} \equiv T_{\rm fit}$, such that its calculation depends on the value of $r/R_{\rm vir,\,host}$:

$$\mathrm{T_{fit}} = 5.62 \sqrt{\frac{R_{\rm vir,host}}{GM_{\rm encl,host}(r)}} r^{0.8} R_{\rm peri}^{0.2} (r < R_{\rm vir,host}),$$

$$\mathrm{T_{fit}} = 5.62 \frac{R_{\rm vir,host}}{\sqrt{GM_{\rm vir,host}}} r^{0.3} R_{\rm peri}^{0.2} (r \geq R_{\rm vir,host}).$$

This new model accurately estimates $\tau_{\rm merge}$ for all infalling haloes and satellites within $3R_{\rm vir,\,host}$.

Based on our analysis, we have drawn the following conclusions:

(i) All currently published models show a strong dependence on $r/R_{\rm vir,\,host}$. For the BT87 and LC93 models, this is because they do not take into account tidal stripping and, in the case of the BT87 model, do not include the effect of the type of orbit the merging system is on. The J08 and BK08 models were calibrated at $r = R_{\rm vir,\,host}$, and so they did not account for the trend with $r/R_{\rm vir,\,host}$.

(ii) The predictions of the LC93 and BK08 models depend on the circular radius $R_{\rm circ}$, which affects not only their median behaviour with radius, but also the size of scatter at fixed radius, which is a consequence of the dependence of $R_{\rm circ} \equiv R_{\rm circ}(E)$ on orbital energy, E.

(iii) This dependence on orbital energy means that both the LC93 and BK08 models overpredict $T_{\rm sim}$ for satellites and haloes on unbound orbits; this is not the case for the BT87 or J08 models, or our new model.

(iv) All currently published models predict $\tau_{\rm merge}$ that show a strong dependence on satellite-to-host mass ratio, underpredicting $\tau_{\rm merge}$ for higher mass systems and overpredicting it for lower mass ones. Our prescription does not show this same behaviour and provides an accurate prediction for all satellite-to-host mass ratios.

(v) The pericentric distance, $R_{\rm peri}$, of a satellite is a more accurate predictor of its type of orbit than the more usual measure of eccentricity, η.

We note that our new model has a limited dependence on satellite mass, $M_{\rm sat}$, which can be removed using the specific energy E and angular momentum L instead. However, this has negligible effects on the accuracy of our model predictions, giving at most a 10 per cent difference for the largest satellites.

Our new model has implications for a wide range of problems in galaxy formation and evolution. As will be shown in future work, an implementation of our new model in the SHARK SAM of galaxy formation (Lagos et al. 2018) has important implications for the contribution of satellite and central galaxies to the stellar mass function. Relative to the standard SHARK model, the numbers of satellites increase at all redshifts and all stellar masses; in contrast, the number of centrals at higher $M_\star$ is suppressed at $z > 0.5$ because of the reduced merger rate, while it is enhanced at $z = 0$ because super massive black holes are less massive and produce weaker feedback, leading to increased star formation rates and higher stellar masses. Further details will be presented in Proctor et al. (in preparation).

We expect our new dynamical friction time-scale to have an impact in a variety of areas, some of which we list next: (i) Because our dynamical friction model affects the numbers of satellite and central galaxies, it is natural to expect changes in the predicted clustering of galaxies in mock galaxy catalogues, which are important for comparison with galaxy surveys (e.g. Robotham et al. 2011).

(ii) The new dynamical friction model presented here can be used to investigate halo–halo merger rates using extended Press–Schechter theory; cosmological simulations have shown that significant amount of dark matter in haloes accumulate via mergers (Wright et al. 2020), and hence an accurate understanding of dynamical friction for reliable predictions is required (Lacey & Cole 1993; Parkinson, Cole & Helly 2008). (iii) We also expect our dynamical friction time-scale to impact scaling relations of haloes, particularly at the regime of groups and clusters, where the satellite population becomes increasingly important. An example of this is the H I–halo mass relation; because H I in high halo mass systems resides predominantly within satellite galaxies, accurate lifetimes for satellites are essential if we are to produce strong theoretical limits on the relation (Chauhan et al. 2020).

Finally, we note that we have focused on the results of dark matter only simulations, but the effect of baryons is non-negligible. Previous studies (Boylan-Kolchin et al. 2008; Dolag et al. 2009; Jiang et al. 2010) have found that baryons can reduce lifetimes of satellites/subhalos by $\approx$10 per cent on average. Why exactly this occurs is interesting. The presence of baryons tends to make subhalos hosting satellites more concentrated, and less susceptible to tidal stripping, which means that they can be exposed to the strong tides associated with the central galaxy within the host for longer – accelerating orbital decay. We hope to investigate further the various factors that influence the merging time-scale in the presence of baryons using hydrodynamical simulations in the future.

ACKNOWLEDGEMENTS

We would like to thank the anonymous referee and Ainulnabilah B. Nasirudin for their assistance in preparing this manuscript. RP is supported by a University of Western Australia Scholarship, while PJE is supported by a PDRA funded by the ARC Centre of Excellence

in All-Sky Astrophysics in 3D (ASTRO 3D). Parts of this research was supported by the Australian Research Council (ARC) Centre of Excellence ASTRO 3D through project number CE170100013. Part of this research was undertaken on Gadi, the NCI National Facility in Canberra, Australia, which is supported by the Australian Government.

DATA AVAILABILITY

The data used in this article were generated using the National Computing Infrastructure (NCI) high performance computing facility in Canberra, Australia. The derived data generated in this research will be shared on reasonable request to the corresponding author.

REFERENCES

Alves J., Combes F., Ferrara A., Forveille T., Shore S., 2016, A&A, 594, E1
Baugh C. M., 2006, Rep. Prog. Phys., 69, 3101
Benson A. J., 2010, Phys. Rep., 495, 33
Binney J., Tremaine S., 1987, Galactic Dynamics. Princeton Univ. Press, Princeton, NJ
Blumenthal G. R., Faber S. M., Flores R., Primack J. R., 1986, ApJ, 301, 27
Boylan-Kolchin M., Ma C. P., Quataert E., 2008, MNRAS, 383, 93
Cañas R., Elahi P. J., Welker C., Lagos C. d. P., Power C., Dubois Y., Pichon C., 2019, MNRAS, 482, 2039
Chandrasekhar S., 1943, Rev. Mod. Phys., 15, a
Chauhan G., Lagos C. D. P., Stevens A. R. H., Obreschkow D., Power C., Meyer M., 2020, MNRAS, 498, 44
Cole S., Lacey C. G., Baugh C. M., Frenk C. S., 2002, MNRAS, 319, 168
Colpi M., Mayer L., Governato F., 1999, ApJ, 525, 720
D'Onghia E., Springel V., Hernquist L., Keres D., 2010, ApJ, 709, 1138
Dayal P., Ferrara A., 2018, Phys. Rep., 780, 1
Deason A., Wetzel A., Garrison-Kimmel S., 2014, ApJ, 794, 115
Dekel A., Devor J., Hetzroni G., 2003, MNRAS, 341, 326
Dolag K., Borgani S., Murante G., Springel V., 2009, MNRAS, 399, 497
Elahi P. J., Thacker R. J., Widrow L. M., 2011, MNRAS, 418, 320
Elahi P. J. et al., 2013, MNRAS, 433, 1537
Elahi P. J., Welker C., Power C., Lagos C. d. P., Robotham A. S., Cañas R., Poulton R., 2018, MNRAS, 475, 5338
Elahi P. J., Cañas R., Poulton R. J., Tobar R. J., Willis J. S., Lagos C. D. P., Power C., Robotham A. S., 2019a, Publ. Astron. Soc. Aust., 36, e021
Elahi P. J., Poulton R. J. J., Tobar R. J., Canas R., Lagos C. d. P., Power C., Robotham A. S. G., 2019b, Publ. Astron. Soc. Aust., 36, e028
Faber S. M., Jackson R. E., 1976, ApJ, 204, 668
Freeman K. C., 1970, ApJ, 160, 811
Gan J. L., Kang X., Hou J. L., Chang R. X., 2010, Res. Astron. Astrophys., 10, 1242
Gnedin O. Y., Hernquist L., Ostriker J. P., 1999, ApJ, 514, 109
Hayashi E., Navarro J. F., Taylor J. E., Stadel J., Quinn T., 2003, ApJ, 584, 541
Jiang C. Y., Jing Y. P., Faltenbacher A., Lin W. P., Li C., 2008, ApJ, 675, 1095
Jiang C. Y., Jing Y. P., Lin W. P., 2010, A&A, 510, A60
Jiang L., Helly J. C., Cole S., Frenk C. S., 2014, MNRAS, 440, 2115
Jiang I.-G., Binney J., 2000, MNRAS, 314, 468
Knebe A. et al., 2011, MNRAS, 415, 2293
Kravtsov A. V., Gnedin O. Y., Klypin A. A., 2004, ApJ, 609, 482
Lacey C., Cole S., 1993, MNRAS, 262, 627
Lagos C. d. P., Tobar R. J., Robotham A. S., Obreschkow D., Mitchell P. D., Power C., Elahi P. J., 2018, MNRAS, 481, 3573
Lee J. et al., 2014, MNRAS, 445, 4197
Miller T. B., van den Bosch F. C., Green S. B., Ogiya G., 2020, MNRAS, 495, 4496
Mo H., van den Bosch F., White S., 2010, Galaxy Formation and Evolution. Cambridge Univ. Press, Cambridge
Muldrew S. I. et al., 2012, MNRAS, 419, 2670
Navarro J. F., Frenk C. S., White S. D. M., 1995, MNRAS, 275, 56
Navarro J. F., Frenk C. S., White S. D. M., 1997, ApJ, 490, 493
Ostriker J. P., Spitzer, Lyman J., Chevalier R. A., 1972, ApJ, 176, L51
Parkinson H., Cole S., Helly J., 2008, MNRAS, 383, 557
Poulton R. J., Robotham A. S., Power C., Elahi P. J., 2018, Publ. Astron. Soc. Aust., 35, e035
Poulton R. J. J., Power C., Robotham A. S. G., Elahi P. J., 2019, MNRAS, 491, 3820
Robotham A. S., Obreschkow D., 2015, Publ. Astron. Soc. Aust., 32, e033
Robotham A. S. et al., 2011, MNRAS, 416, 2640
Rubin V. C., Thonnard N., Ford W. K. J., 1980, ApJ, 238, 471
Simha V., Cole S., 2017, MNRAS, 472, 1392
Somerville R. S., Davé R., 2015, ARA&A, 53, 51
Srisawat C. et al., 2013, MNRAS, 436, 150
Taffoni G., Mayer L., Colpi M., Governato F., 2003, MNRAS, 341, 434
Taylor J. E., Babul A., 2004, MNRAS, 348, 811
Toomre A., 1977, Tinsley B. M., Larson R. B., Proceedings of a Conference at Yale University , Evolution of Galaxies and Stellar Populations, Yale University Observatory, New Haven. p. 401
van den Bosch F. C., Ogiya G., 2018, MNRAS, 475, 4066
van den Bosch F. C., Ogiya G., Hahn O., Burkert A., 2018, MNRAS, 474, 3043
Velazquez H., White S. D. M., 1999, MNRAS, 304, 254
Wetzel A. R., White M., 2010, MNRAS, 403, 1072
White S. D. M., Rees M. J., 1978, MNRAS, 183, 341
Wright R. J., Lagos C. d. P., Power C., Mitchell P. D., 2020, MNRAS, 498, 1668
Zentner A. R., Berlind A. A., Bullock J. S., Kravtsov A. V., Wechsler R. H., 2005, ApJ, 624, 505

APPENDIX A: VARIATION OF PERICENTRIC RADIUS WITH HOST VIRIAL RADIUS

The change in the magnitude of the radial velocity relative to the circular velocity, $V_{\rm rad}/V_{\rm circ}$, as a function of $r/R_{\rm vir,\,host}$, is shown in Fig. A1. Objects on smoothly inspiralling orbits should have a constant $V_{\rm rad}/V_{\rm circ}$ with a value $\sim$1, which is not observed in Fig. A1. The value for $V_{\rm rad}/V_{\rm circ}$ is greater than unity and varies with position, demonstrating that these objects tend to be on more radial orbits as they cross the region from 3 $R_{\rm vir,\,host}$ to 1 $R_{\rm vir,\,host}$. This tendency to be on more radial orbits implies that the time to cross this region

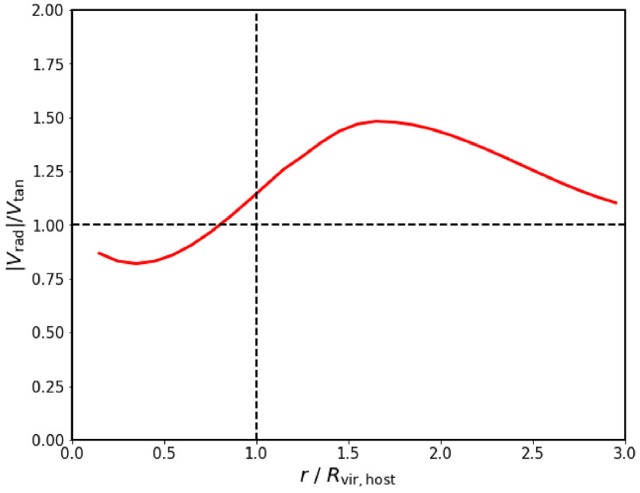

Figure A1. Variation of the ratio of the magnitude of radial velocity $|V_{\rm rad}|$ over the tangential velocity $V_{\rm tan}$ as a function of $r/R_{\rm vir,\,host}$. The red line shows the median in each $r/R_{\rm vir,\,host}$ bin. The vertical dashed line shows when $r = R_{\rm vir,\,host}$, while the horizontal dashed line shows where $|V_{\rm rad}| = V_{\rm tan}$.

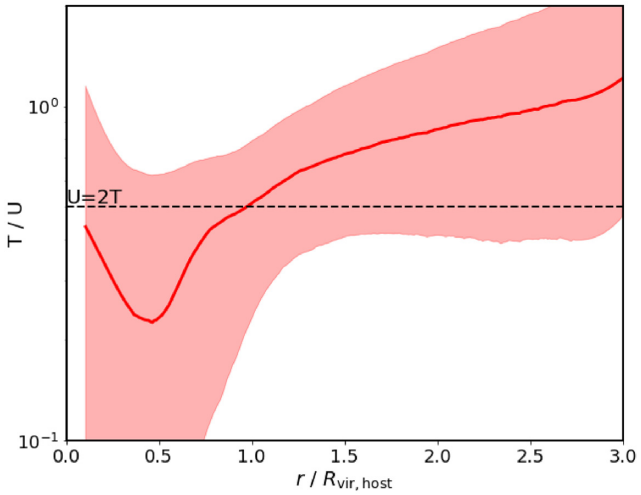

Figure B1. Variation of the ratio of satellites' kinetic to potential energy with $r/R_{\rm vir,\,host}$, where the red line shows the median in each $r/R_{\rm vir,\,host}$ bin and the shaded region shows the standard deviation. The black-dashed line indicates the region where we would expect to find satellites that follow the virial theorem (i.e. U = 2T).

will be less than predicted assuming that the object is on a smoothly inspiralling orbit.

APPENDIX B: VIRIAL THEOREM

Fig. B1 shows how the ratio of the kinetic to potential energy of satellites changes with $r/R_{\rm vir,\,host}$. The dashed line shows where the virial theorem is valid (U = 2T). Most satellites at large radii have U > 2T and this holds true until they pass within $R_{\rm vir,host}$, at which point the virial theorem holds for the satellite. However, as the satellite passes within $R_{\rm vir,host}$, it becomes more bound and so U/T decreases until $0.5R_{\rm vir,host}$, at which point the small enclosed mass within the orbit of the satellite leads to U/T increasing.

APPENDIX C: ORBIT PREDICTOR

The ideal properties for an orbit predictor are

(i) its value should change with $T_{\rm sim}$, demonstrating that it can predict whether an object is on a stable orbit with a long $T_{\rm sim}$ or is on highly radial orbit with a short $T_{\rm sim}$; and
(ii) there is limited scatter in its value because increased scatter leads to a larger uncertainty in $T_{\rm model}$.

We demonstrate some of the key orbit predictors explored in this work in Fig. C1, where the top panel shows how the $R_{\rm circ}/R_{\rm vir,\,host}$ changes as a function of $T_{\rm sim}$. $R_{\rm circ}/R_{\rm vir,\,host}$ is broadly insensitive to $T_{\rm sim}$, which shows that it does not satisfy condition (i); it also has a large scatter in its value, which shows that it does not satisfy condition (ii). In contrast, η (middle panel) shows a slight variation with $T_{\rm sim}$, and so somewhat satisfies condition (i), while its reduced scatter satisfies condition (ii). However, we find that the best-performing orbit predictor is $R_{\rm peri}/r$, which

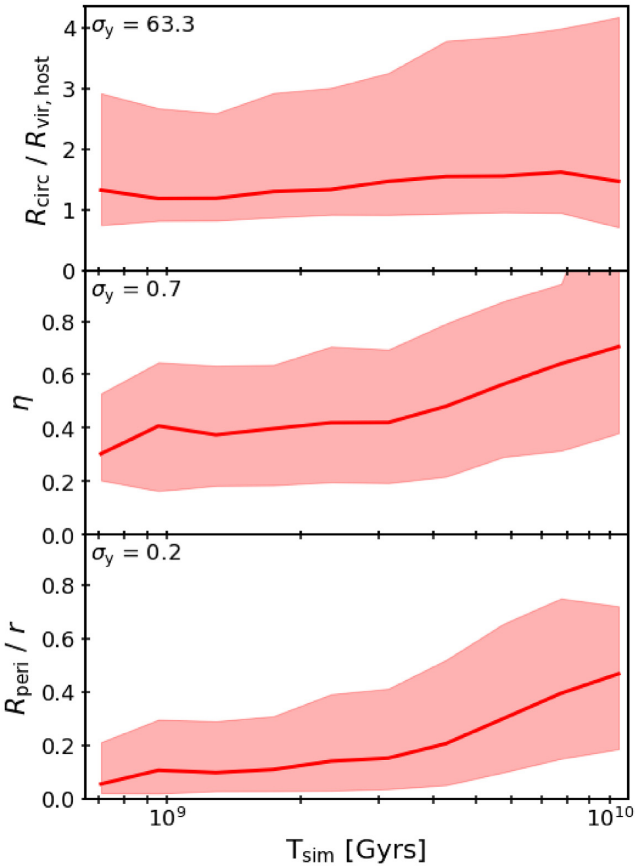

Figure C1. Variation of $R_{\rm peri}/r$, η, and $R_{\rm circ}/R_{\rm vir,\,host}$ with simulation merger time-scale $T_{\rm sim}$, as computed at infall. The red line shows the median in each $T_{\rm sim}$ bin and the shaded region shows the standard deviation. The text in the top left of each panel shows the standard deviation along the y-axis.

shows the largest variation with $T_{\rm sim}$ and the least amount of scatter.

APPENDIX D: SATELLITE SELECTION CRITERIA

In this section, we evaluate the selection criteria for infalling satellite. Fig. D1 shows how $T_{\rm sim}$ calculated at infall [$T_{\rm sim}(R_{\rm vir,\,host})$] changes with where the satellite merges within its host ($\frac{r_{\rm merge}}{R_{\rm vir,host}}$) and the number of particles the satellite had at infall ($N_{\rm part,\,sat,\,infall}$) for all satellites that have $N_{\rm part,\,sat,\,infall} > 100$. From the figure, there is a slight bias towards longer $T_{\rm sim}(R_{\rm vir,\,host})$ by selecting satellites that merge within 0.1 $R_{\rm vir,\,host}$. This bias, however, is only minor if selecting satellites that have $N_{\rm part,\,sat,\,infall} > 1000$. Furthermore, the right-hand panel in Fig. D1 shows that the selection of $N_{\rm part,\,sat,\,infall}$ >1000 cause little-to-no bias in $T_{\rm sim}(R_{\rm vir,\,host})$.

In Fig. D2, the top panel shows the PDF of where satellites with $N_{\rm part,\,sat,\,infall}$ >1000, merge within $R_{\rm vir,\,host}$. From the plot it is evident that the selection of $0.1R_{\rm vir,\,host}$ captures the vast majority of satellites, with very few merging outside $0.1R_{\rm vir,\,host}$. We note that there is a small population of mergers outside $0.1R_{\rm vir,\,host}$, which is most like due to satellite–satellite interaction. The bottom panel shows ratio of

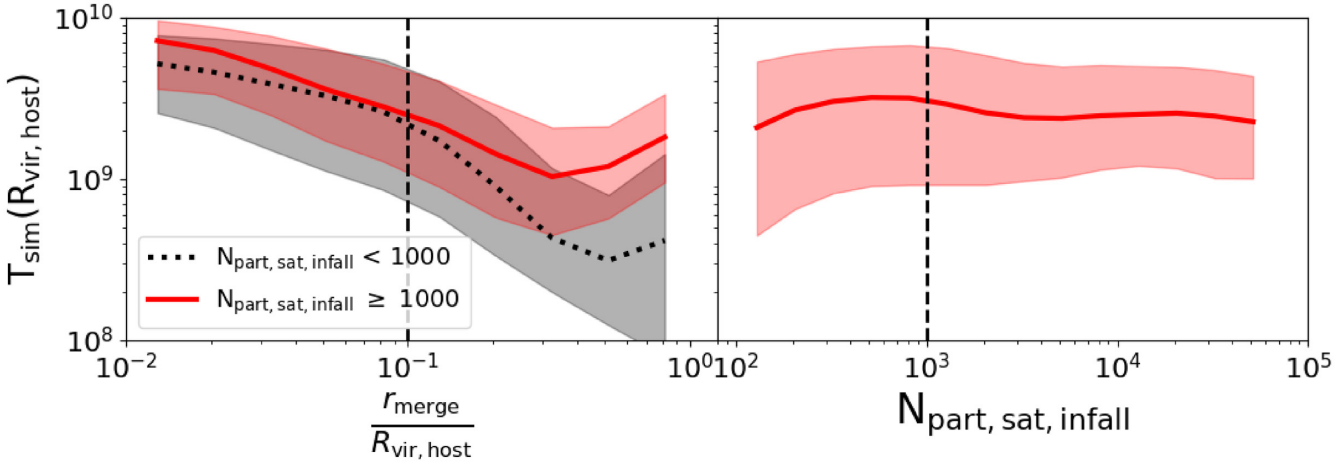

Figure D1. The left-hand panel shows how the T_{sim} calculated at infall [$T_{sim}(R_{vir,\,host})$] varies as a function of where it merges within its host($\frac{r_{merge}}{R_{vir,host}}$) , where the solid red line shows the medians for satellites with $N_{part,\,sat,\,infall} \geq 1000$ and the dotted black line shows for satellites with $N_{part,\,sat,\,infall} < 1000$. The shaded regions shows the standard deviations for each selection. The right-hand panel shows how $T_{sim}(R_{vir,\,host})$ varies with $N_{part,\,sat,\,infall}$, the solid red line shows the median, and the shaded region shows the standard deviation. In both panels, a selection of $N_{part,\,sat,\,infall} \geq 100$ is also applied to remove unresolved satellites.

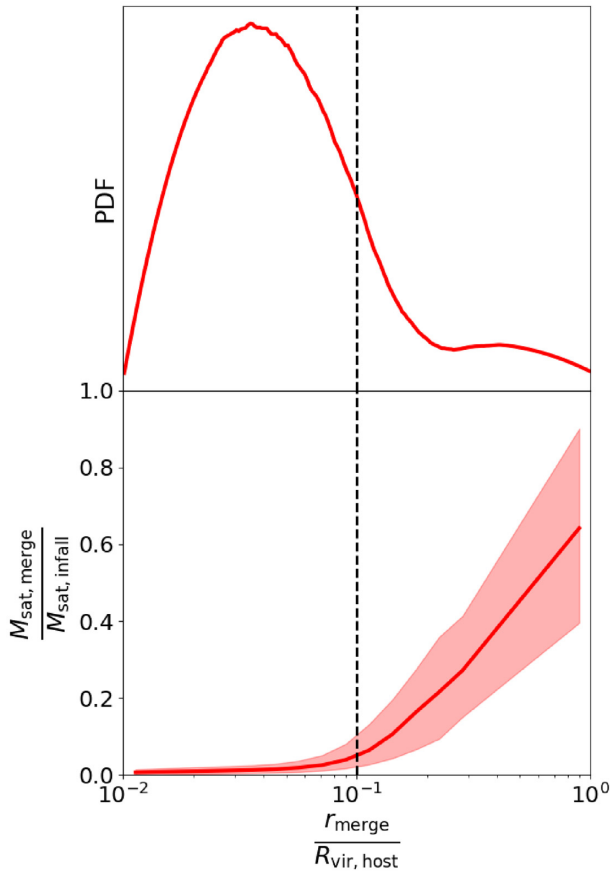

Figure D2. The top panel shows a PDF of where satellites merge within $R_{vir,\,host}$ ($\frac{r_{merge}}{R_{vir,host}}$). The bottom panel shows the ratio of the mass that satellites merge with to the mass at infall as a function of $\frac{r_{merge}}{R_{vir,host}}$, where the red line is the median and the shaded region is the standard deviation. The vertical dashed line shows the merger selection criteria.

the mass the satellite merged with $M_{sat,\,infall}$ to the mass of the satellite at infall $M_{sat,\,infall}$ for satellites with $N_{part,\,sat,\,infall} > 1000$ as a function of where they merge within $R_{vir,\,host}$. From the plot, satellites lose over 95 per cent of their mass when they merge within $0.1R_{vir,\,host}$, meaning that these satellites have fully merged with their host.

APPENDIX E: CONVERGENCE TEST

To test the applicability of the new formula to other simulations, we apply it to a lower resolution 40 h^{-1} Mpc box with 512^3 particles from the Synthetic UniveRses For Surveys (Elahi et al. 2018) suite of simulations (with the same cosmology). We apply the same selection for infalling satellites by applying a mass cut of $1.73 \times 10^{10}\,M_{\odot}$,[10] with all other selections the same. Fig. E1 shows the comparison of T_{fit}/T_{sim} for the two simulations, where both simulations overlap at all $r/R_{vir,\,host}$ and have very similar scatter, with the higher resolution having slightly more scatter due to probing more types of satellites orbits.

[10] 1000 particles at infall for the 105 h^{-1} Mpc box with 2048^3 particles, which corresponds to 419 particles in the 40 h^{-1} Mpc box with 512^3 particles.

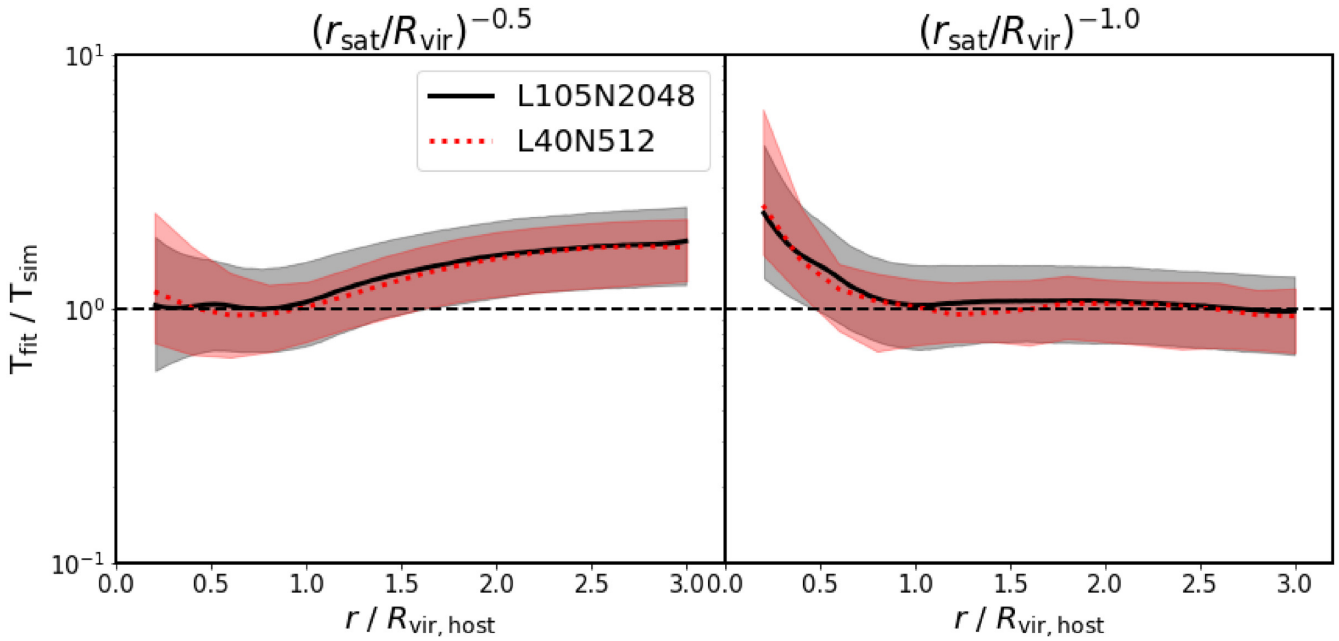

Figure E1. Plots showing the ratio of T_{fit} to T_{sim} for both the lower resolution 40 h^{-1} Mpc box with 512^3 particles (L40N512, the red-dotted line) and the higher resolution 105 h^{-1} Mpc box with 2048^3 particles (L105N2048, the black solid line). For both,the lines are the medians and the shaded region shows the standard deviation. Each panel shows the different functional form, where the left-hand panel shows equation (11) and the right-hand panel shows equation (12).

This paper has been typeset from a TEX/LATEX file prepared by the author.